Steady-State Thermal Modeling of a Power Module: An N-Layer Fourier Approach

Khaled Redwan Choudhury and Daniel J. Rogers, *Member, IEEE*

***Abstract*—The steady-state thermal modeling of a rectangular N-layer structure with an arbitrary number of heat sources on the top surface is obtained by a Fourier series solution. As the structure of power modules can be closely approximated as a rectangular N-layer structure, this model may be used to accurately estimate the temperature field occurring in such modules. Various simplified structures are analyzed to understand the effects of structural approximation on the temperature field. The Fourier-based method developed in this work is compared with the finite-element method simulation, and an excellent matching (approximately 0.27% temperature error) is found in the centers of the semiconductor dies. Experimental temperature measurements taken at the surface of a commercial SiC power module are also presented, demonstrating agreement in the centers of the dies to within 3.5%.**

***Index Terms*—Fourier series, power modules, simulation, thermal modeling, verification.**

NOMENCLATURE

i	Layer number (1,2,...,N).
m	Index of the summation for the eigenvalues of the Fourier expansion in the x-direction (1,2,...,N_m).
n	Index of the summation for the eigenvalues of the Fourier expansion in the y-direction (1,2,...,N_n).
a, b, c, d	Linear dimensions (m).
A_{i0}, B_{i0}	Zeroth-order Fourier coefficients.
A_{im}, B_{im}	Mth Fourier coefficients describing the temperature variation in the x-direction for a constant z.
A_{in}, B_{in}	Nth Fourier coefficients describing the temperature variation in the y-direction for a constant z.
A_{imn}, B_{imn}	Fourier cross-coefficients.
λ_m	Eigenvalues of the Fourier expansions in the x-direction (m^{-1}).
δ_n	Eigenvalues of the Fourier expansions in the y-direction (m^{-1}).
β_{mn}	Eigenvalues of the cross-coupled Fourier expansions (m^{-1}).
h	Convection coefficient at the bottom surface ($\mathrm{W}/(\mathrm{m}^2 \cdot \mathrm{K})$).

Manuscript received January 25, 2018; accepted March 29, 2018. Date of publication April 18, 2018; date of current version December 7, 2018. Recommended for publication by Associate Editor S. S. Ang. *(Corresponding author: Khaled Redwan Choudhury.)*

The authors are with the Energy and Power Group, University of Oxford, Oxford OX1 2JD, U.K. (e-mail:

an isothermal surface is demonstrated. An analytical solution is proposed in [12] to calculate the thermal spreading resistance for rectangular sources on rectangular substrates. A general solution of a steady-state temperature rise due to an arbitrary number of heat sources situated on a rectangular single-layer structure and a double-layer structure is proposed in [13]. The work in [13] is extended in [14] to include the effect of interfacial resistance in a rectangular double-layer structure with a very thin interfacial layer between them. Analytical solutions have also been developed for systems with four layers using Green's functions in [15]. In [16], a general solution for the temperature rise in multilayer rectangular domains with nonuniform internal heat generation is presented. Although applicable in many problems, this technique requires manipulation of a large sparse matrix to determine the Fourier coefficients, which may be computationally very demanding depending upon the number of layers. These analytical or meshless solutions, although useful, have not found much application in power electronics. For example, in [17], analytical thermal modeling for a central circular heat source situated on a cylindrical power module with three layers is presented. However, in practice, cylindrical power modules and circular semiconductor devices are not often seen (apart from high-power thyristor-type devices). Moreover, there are almost always more than three layers in practical power modules. In [18] and [19], Fourier-series-based techniques are used, but the presented method does not directly solve Laplace's equation for each layer; rather, the whole system is implemented as a chain of blocks in MATLAB/Simulink.

In this paper, steady-state thermal modeling of a rectangular structure with an arbitrary number of layers containing an arbitrary number of rectangular heat sources on its topmost surface is presented. This method is then applied to the power module. The model is verified using the FEM package COMSOL Multiphysics and by the experiment. The major advantage of the method presented in this paper over mesh methods, such as the FEM, is that it can evaluate the temperature of a single point quickly, in contrast to mesh methods, where the entire temperature field must be found. In addition, Fourier-based methods are smooth with dimensional changes, and hence, it may be readily applied to the numerical optimization of power module designs using standard optimization frameworks.

II. Problem Statement

At first, let us consider a rectangular structure with N different layers containing only one rectangular heat source, as shown in Fig. 1 (the effect of multiple heat sources will be considered later). The thickness and the thermal conductivity of the ith layer of the rectangular structure are t_i and k_i, respectively. The bottom surface of the structure has a convection coefficient h and is cooled convectively by a cooling fluid of uniform temperature T_f. The rectangular heat source is situated on the surface of layer 1. The position of the source is given by its center $(X_C, Y_C, 0)$ and its length and width are c and d, respectively. This source generates heat Q uniformly

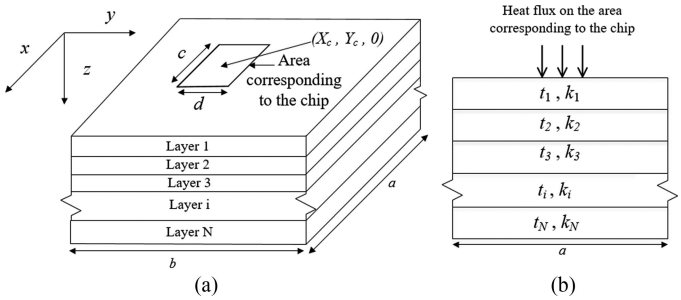

Fig. 1. (a) Schematic of an N-layer structure. (b) Side view of the structure with heat flux.

over the surface it is situated. It is also assumed that all the surfaces of the rectangular structure are adiabatic (insulated) except the bottom surface, which is subject to the convective boundary condition. The governing equation of the system is Laplace's

$$\frac{\partial^2 \theta_i}{\partial x^2} + \frac{\partial^2 \theta_i}{\partial y^2} + \frac{\partial^2 \theta_i}{\partial z^2} = 0. \tag{1}$$

Underneath the heat source, the first layer is subject to the boundary condition (2):

$$\left.\frac{\partial \theta}{\partial z}\right|_{z=0} = -\frac{Q}{k_1 cd}. \tag{2}$$

Outside the source, the boundary condition is

$$\left.\frac{\partial \theta}{\partial z}\right|_{z=0} = 0. \tag{3}$$

Considering the perfect contact between the layers, the boundary conditions at the interfaces are

$$k_i \left.\frac{\partial \theta_i}{\partial z}\right|_{z=z_i} = k_{i+1} \left.\frac{\partial \theta_{i+1}}{\partial z}\right|_{z=z_i} \tag{4}$$

and

$$\theta_i(x, y, z_i) = \theta_{i+1}(x, y, z_i) \tag{5}$$

where

$$z_i = \sum_{j=1}^{i} t_j.$$

The boundary condition for the bottom layer is

$$k_N \left.\frac{\partial \theta_N}{\partial z}\right|_{z=z_N} = -h\theta_N|_{z=z_N}. \tag{6}$$

III. Problem Solution: Rectangular N-Layer Fourier (RNLF) Method

A. Top Layer (Layer 1)

The governing equation and all the boundary conditions are homogeneous except (2). Therefore, this problem can be solved

by the separation of variables method [20]. The solution can be expressed as

$$\begin{aligned}\theta_i(x,y,z) &= A_{i0} + B_{i0}z \\ &+ \sum_{m=1}^{\infty}\cos(\lambda_m x)[A_{im}\cosh(\lambda_m z) + B_{im}\sinh(\lambda_m z)] \\ &+ \sum_{n=1}^{\infty}\cos(\delta_n y)[A_{in}\cosh(\delta_n z) + B_{in}\sinh(\delta_n z)] \\ &+ \sum_{m=1}^{\infty}\sum_{n=1}^{\infty}\cos(\lambda_m x)\cos(\delta_n y)[A_{imn}\cosh(\beta_{mn} z) \\ &+ B_{imn}\sinh(\beta_{mn} z)] \end{aligned} \tag{7}$$

where $\lambda_m = m\pi/a$, $\delta_n = n\pi/b$, and $\beta_{mn} = \sqrt{(\lambda_m^2 + \delta_n^2)}$. Considering the first layer boundary conditions (2) and (3), we have

$$\begin{aligned}\left.\frac{\partial\theta}{\partial z}\right|_{z=0} &= B_{10} + \sum_{m=1}^{\infty} B_{im}\lambda_m\cos(\lambda_m x) \\ &+ \sum_{n=1}^{\infty} B_{1n}\delta_n\cos(\delta_n y) + \sum_{m=1}^{\infty}\sum_{n=1}^{\infty}\beta_{1mn}\cos(\lambda_m x)\cos(\delta_n y).\end{aligned} \tag{8}$$

Now, consider the following integration over the surface $z = 0$ for the x-direction coefficients:

$$\begin{aligned}&\int_0^a\int_0^b\left(\left.\frac{\partial\theta}{\partial z}\right|_{z=0}\right)\cos(\lambda_m x)dxdy \\ &= \lambda_m B_{1m}\int_0^a\int_0^b\cos^2(\lambda_m x)dxdy\end{aligned}$$

Therefore,

$$\begin{aligned}&\int_{X_c-c/2}^{X_c+c/2}\left(-\frac{Q}{k_1 cd}\right)\cos(\lambda_m x)\mathrm{d}x\int_{Y_c-d/2}^{Y_c+d/2}dy \\ &= B_{1m}\int_0^a\cos^2(\lambda_m x)dx\int_0^b dy.\end{aligned}$$

Hence, it follows that

$$B_{1m} = \frac{-4Q\cos(\lambda_m X_c)\sin(\lambda_m c/2)}{abck_1\lambda_m^2}. \tag{9}$$

Similarly, in the y-direction, we have

$$B_{1n} = \frac{-4Q\cos(\delta_n Y_c)\sin(\delta_n d/2)}{abdk_1\delta_n^2}. \tag{10}$$

For the cross-coefficient B_{1mn}, we have

$$B_{1mn} = \frac{-16Q\cos(\lambda_m X_c)\sin(\lambda_m c/2)\cos(\delta_n Y_c)\sin(\delta_n d/2)}{abcdk_1\lambda_m\delta_n\beta_{mn}}. \tag{11}$$

For B_{10}, we have

$$\int_{X_c-c/2}^{X_c+c/2}\left(-\frac{Q}{cd}\right)dx\int_{Y_c-d/2}^{Y_c+d/2}dy = k_1 B_{10}\int_0^a dx\int_0^b dy.$$

Therefore

$$B_{10} = \frac{-Q}{k_1 ab}. \tag{12}$$

The other Fourier coefficients (A_{1m}, A_{1n}, A_{1mn}, and A_{10}) can be determined from the boundary conditions (4)–(6), which is explained in the following sections.

B. Bottom Layer

For the bottom (Nth) layer, the following relation can be obtained from (6):

$$\begin{aligned}&\frac{-h}{k_N}\Big[A_{Nm}\cosh(\lambda_m z_N) + B_{Nm}\sinh(\lambda_m z_N)\Big] \\ &= A_{Nm}\lambda_m\sinh(\lambda_m z_N) + B_{Nm}\lambda_m\cosh(\lambda_m z_N).\end{aligned}$$

Therefore,

$$B_{Nm} = -\sigma_N(\lambda_m)A_{Nm} \tag{13}$$

where

$$\sigma_N(\lambda_m) = \frac{\lambda_m\sinh(\lambda_m z_N) + h/k_N\cosh(\lambda_m z_N)}{\lambda_m\cosh(\lambda_m z_N) + h/k_N\sinh(\lambda_m z_N)}.$$

It should be mentioned that $\sigma_N(\delta_n)$ and $\sigma_N(\beta_{mn})$ can be obtained by replacing λ_m with δ_n and β_{mn}, respectively. If the convection coefficient h is very large, the bottom surface becomes isothermal. In this case, we have

$$\sigma_N(\lambda_m) = \coth(\lambda_m z_N). \tag{14}$$

C. Middle Layers ($i < N$)

The interface boundary conditions (4) and (5) are applied in the middle layers. To illustrate the process, let us consider a three-layer structure. In the interface between the first and second layers, the following relation can be obtained from (4):

$$\begin{aligned}&A_{2m}\sinh(\lambda_m t_1) + B_{2m}\cosh(\lambda_m t_1) \\ &= k_1/k_2(A_{1m}\sinh(\lambda_m t_1) + B_{1m}\cosh(\lambda_m t_1)).\end{aligned} \tag{15}$$

From (5), we obtain

$$\begin{aligned}&A_{2m}\cosh(\lambda_m t_1) + B_{2m}\sinh(\lambda_m t_1) \\ &= A_{1m}\cosh(\lambda_m t_1) + B_{1m}\sinh(\lambda_m t_1).\end{aligned} \tag{16}$$

Now, (16) $\times\cosh(\lambda_m t_1)$ – (15) $\times\sinh(\lambda_m t_1)$ yields

$$A_{2m} = A_{1m}\phi_1 + B_{1m}\psi_1 \tag{17}$$

where

$$\phi_1 = \cosh^2(\lambda_m t_1) - k_1/k_2\sinh^2(\lambda_m t_1)$$

and

$$\psi_1 = \sinh(\lambda_m t_1)\cosh(\lambda_m t_1)(1 - k_1/k_2).$$

Similarly,

$$B_{2m} = -(A_{1m}\psi_1 + B_{1m}\rho_1) \tag{18}$$

where

$$\rho_1 = \sinh^2(\lambda_m t_1) - k_1/k_2\cosh^2(\lambda_m t_1).$$

Similarly, it can be shown that for other layers

$$A_{3m} = A_{2m}\phi_2 + B_{2m}\psi_2 \tag{19}$$

$$B_{3m} = -(A_{2m}\psi_2 + B_{2m}\rho_2) \tag{20}$$

where

$$\phi_2 = \cosh^2(\lambda_m(t_1+t_2)) - k_2/k_3\sinh^2(\lambda_m(t_1+t_2))$$

$$\psi_2 = \sinh(\lambda_m(t_1+t_2))\cosh(\lambda_m(t_1+t_2))(1-k_2/k_3)$$

and

$$\rho_2 = \sinh^2(\lambda_m(t_1+t_2)) - k_2/k_3\cosh^2(\lambda_m(t_1+t_2)).$$

Now, from (19) and (20), we obtain

$$\frac{B_{3m}}{A_{3m}} = \frac{-(A_{2m}\psi_2 + B_{2m}\rho_2)}{A_{2m}\phi_2 + B_{2m}\psi_2}.$$

From (13), we obtain

$$\sigma_3 = \frac{(A_{2m}\psi_2 + B_{2m}\rho_2)}{A_{2m}\phi_2 + B_{2m}\psi_2}. \tag{21}$$

Hence, from (21), it follows that

$$\sigma_2 = \frac{-B_{2m}}{A_{2m}} = \frac{\sigma_3\phi_2 - \psi_2}{\sigma_3\psi_2 - \rho_2}. \tag{22}$$

Similarly,

$$\sigma_1 = \frac{-B_{1m}}{A_{1m}} = \frac{\sigma_2\phi_1 - \psi_1}{\sigma_2\psi_1 - \rho_1}. \tag{23}$$

This process may be repeated for successive layers in the case of an N-layer structure, i.e., σ_i may be found from

$$\sigma_i = \frac{-B_{im}}{A_{im}} = \frac{\sigma_{i+1}\phi_i - \psi_i}{\sigma_{i+1}\psi_i - \rho_i} \tag{24}$$

where

$$\phi_i = \cosh^2\left(\lambda_m\sum_{j=1}^{i}t_j\right) - k_i/k_{i+1}\sinh^2\left(\lambda_m\sum_{j=1}^{i}t_j\right)$$

$$\psi_i = \sinh\left(\lambda_m\sum_{j=1}^{i}t_j\right)\cosh\left(\lambda_m\sum_{j=1}^{i}t_j\right)(1-k_i/k_{i+1})$$

and

$$\rho_i = \sinh^2\left(\lambda_m\sum_{j=1}^{i}t_j\right) - k_i/k_{i+1}\cosh^2\left(\lambda_m\sum_{j=1}^{i}t_j\right).$$

Thus, (24) provides a route to calculate all σ_i starting from σ_{N-1}, σ_{N-1} from σ_N, σ_{N-2} from σ_{N-1}, σ_{N-3} from σ_{N-2}, and so on. Once σ_1 is obtained by this successive substitution method, A_{1m} is obtained from (21) as B_{1m} is directly calculated from (9). Similarly, $\sigma_1(\delta_n)$ and $\sigma_1(\beta_{mn})$ can be obtained, which can be used to calculate A_{1n} and A_{1mn} directly. A block diagram is given in Fig. 2 to illustrate this process.

It now only remains to find A_{10}. For the sake of simplicity, a two-layer structure is considered. From the convective boundary condition, the following relation is obtained:

$$-(h/k_2)A_{20} = B_{20}(1 + h(t_1+t_2)/k_2). \tag{25}$$

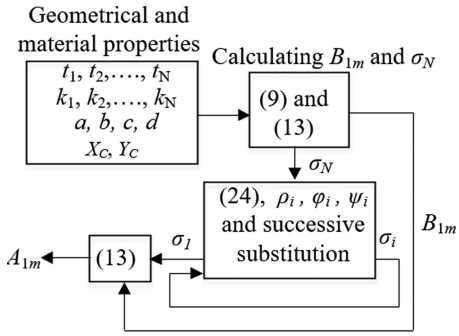

Fig. 2. Process to determine A_{1m}.

From the interface boundary condition (4), we have

$$k_1B_{10} = k_2B_{20}. \tag{26}$$

From (12), we obtain

$$B_{20} = \frac{-Q}{k_2ab}. \tag{27}$$

Now, substituting B_{20} into (25) gives

$$A_{20} = \frac{Q}{ab}\left(\frac{t_1+t_2}{k_2} + \frac{1}{h}\right). \tag{28}$$

Again, from (5), we obtain

$$A_{10} + B_{10}t_1 = A_{20} + B_{20}t_1.$$

Hence,

$$A_{10} = \frac{Q}{ab}\left(\frac{t_1}{k_1} + \frac{t_2}{k_2} + \frac{1}{h}\right). \tag{29}$$

Similarly, for an N-layer structure, it can be shown that

$$A_{10} = \frac{Q}{ab}\left[\left(\sum_{i=1}^{N}\frac{t_i}{k_i}\right) + \frac{1}{h}\right]. \tag{30}$$

As the heat transfer problem is linear, if multiple heat sources are present, the temperature field is obtained simply by the summation of the individual temperature field produced by each heat source considered alone.

IV. Application of the Thermal Model of an N-Layer Structure to a Power Module

A. Structure of the Power Electronic Module

Fig. 3 shows the schematic of the cross-sectional view of a typical power module attached to a heatsink. Thermal grease is used as an interfacing material between the module and the heatsink. The heatsink may be cooled by forced air convection or liquid cooling. The baseplate is typically made of copper. The substrate layer is made of electrically insulated but thermally conductive material such as Al_2O_3 or Si_3N_4. The top view of the power module studied in this paper (Microsemi Power Module Products, part no. APTMC120AM20CT1NG) is shown in Fig. 4. Relevant dimensions and material properties are given in Table I.

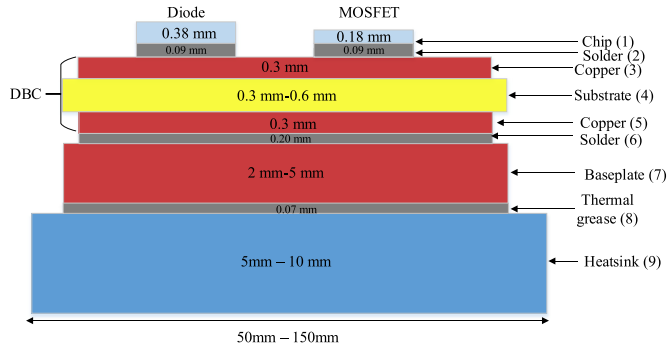

Fig. 3. Schematic of the cross-sectional view of a typical power module with heatsink.

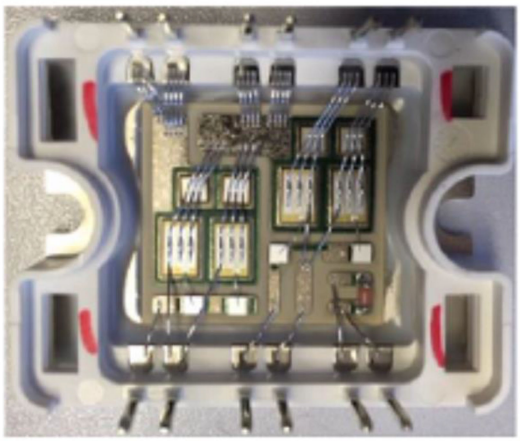

(a)

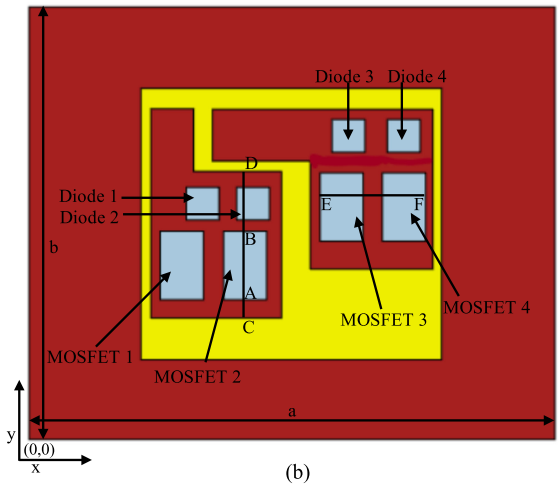

(b)

Fig. 4. (a) Top view of a commercial power module (courtesy of Microsemi Power Module Products). (b) Equivalent schematic view showing the devices (heat sources) and the lines AB, CD, and EF.

B. RNLF Method and the Simulation of Different Structures

The RNLF method assumes that all layers occupy the full extent of the rectangular surface. However, in real power modules, the top copper layer of the direct bonded copper (DBC) stack is patterned, and the substrate is smaller than the baseplate. Therefore, in order to justify the application of the RNLF method to the modeling of power modules, it must be argued

TABLE I
MATERIAL ASSEMBLY AND THE RELEVANT PROPERTIES OF THE SiC POWER MODULE (COURTESY OF MICROSEMI POWER MODULE PRODUCTS)

Layers (Fig. 3)	Material	Size (mm^2)	Thickness (mm)	k (W/m/K)
1	SiC MOSFET	4.04×6.44	0.18	370
	SiC Diode	3.08×3.08	0.377	370
2	MOSFET solder	4.04×6.44	0.09	30
	Diode solder	3.08×3.08	0.09	30
3	Copper	28.2×25.54	0.3	390
4	Si_3N_4 (Substrate)	28.2×25.54	0.32	90
5	Copper	28.2×25.54	0.3	390
6	Solder	28.2×25.54	0.2	30
7	Copper (Baseplate)	49.46×40.8	2.5	390
8	Thermal grease	49.46×40.8	0.10	2.5

TABLE II
DIFFERENT STRUCTURES FOR SIMULATION

Copper	Dissipation	Solder	Structure-acronyms	Fig. no.
Patterned	Volume	Under the die area only	PVU	5
Patterned	Area	Under the die area only	PAU	6
Continuous	Volume	Under the die area only	CVU	7
Continuous	Area	Under the die area only	CAU	8
Continuous	Area	Thermal Resistance	CAR	8
Continuous	Area	Continuous	CAC	9

that the patterning and the limited extent of the DBC stack does not greatly affect the temperature field, particularly in the key regions around the die. The solder layer and the DBC stack are very thin compared to their lengths and widths. Hence, it is reasonable to assume that heat spreading in these layers occurs only near the edges of the dies and does not extend far beyond them. To verify this assumption, a number of COMSOL FEM models are used to investigate the effects of the simplifications required to reduce the complex power module to a simpler structure, which can be solved using the RNLF method. The simplified structures are classified based on three features: copper layer type, dissipation type (area or volume), and solder layer type. *Area dissipation* means there is no die and all the heat enters the corresponding chip area perpendicularly to the surface. *Volume dissipation* means the presence of the die with internal heat generation. The simplified structures are described in Table II. In this work, a relatively thick heat spreader of aluminum alloy is used to create an isothermal surface as the boundary condition at the bottom of the heat spreader (thick blue block in Figs. 5–9), which will be discussed later.

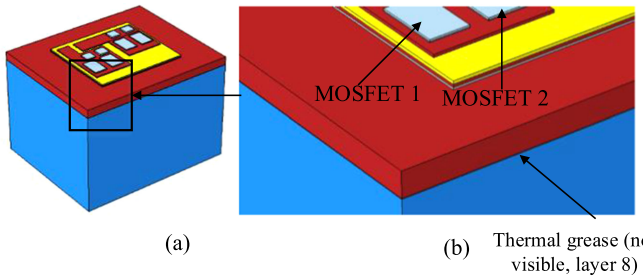

Fig. 5. (a) Three-dimensional view of the PVU. (b) Magnified view of the upper part of the structure.

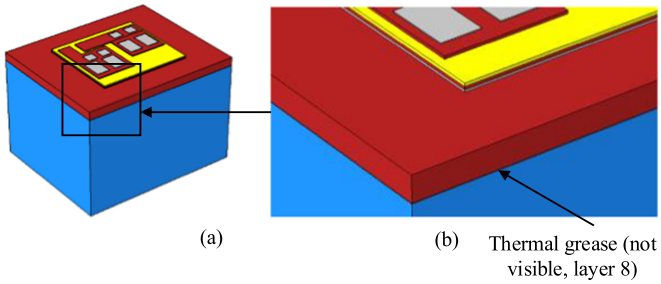

Fig. 6. (a) Three-dimensional view of the PAU. (b) Magnified view of the upper part of the structure.

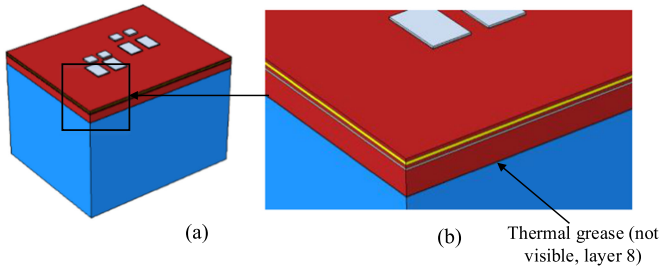

Fig. 7. (a) Three-dimensional view of the CVU. (b) Magnified view of the upper part of the structure.

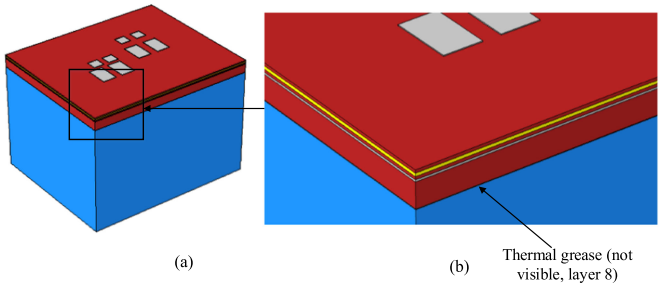

Fig. 8. (a) Three-dimensional view of both the CAU and the CAR. (b) Magnified view of the upper part of the structure.

Figs. 5–7 show the relevant diagrams of the PVU, PAU, and CVU structures, respectively. Fig. 8 shows both the CAU and the CAR structures. Fig. 9 shows the CAC structure, which corresponds to the RNFL method.

1) Simulation Results and Relevant Discussion: The temperatures of the MOSFET devices are of particular interest because these typically represent the hottest, mostly thermally sensitive, devices. Therefore, in Fig. 10, the temperature profile

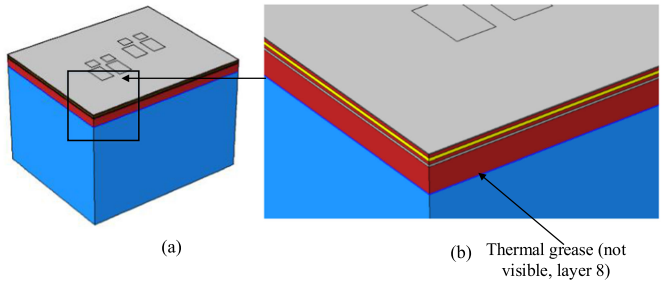

Fig. 9. (a) Three-dimensional view of the CAC. (b) Magnified view of the upper part of the structure.

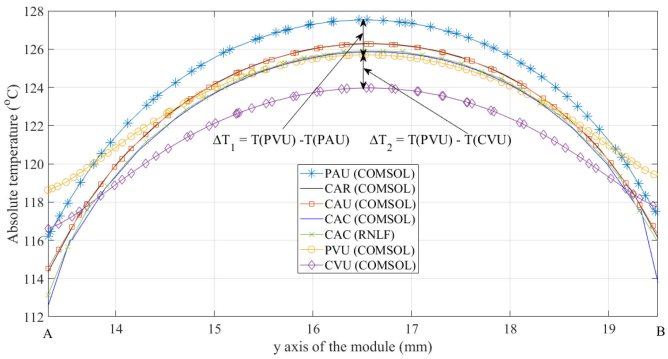

Fig. 10. Comparison of the simulation results for different structures along the line AB ($N_m = N_n = 200$ for CAC RNLF).

along the line AB in Fig. 4(b) ($x = 20.152$ mm), which cuts through MOSFET 2 over the solder layer, is selected for a detailed examination. It should be noted that the side view of AB for the COMSOL FEM (PVU) model is different from the side view of AB in the RNLF method (see Fig. 17). All temperatures are calculated on the top surface of the solder (just underneath the die). This closely reflects the die temperature because the temperature within the die is almost constant due to the high thermal conductivity of SiC.

The PAU structure demonstrates higher temperature compared to the PVU structure except at the edges of the dies. The only difference between the PAU and the PVU structures is the presence of dies. Therefore, it can be concluded that in the structure corresponding to the PVU, there is some heat spreading within the die such that heat flux is not normal on the top surface of the solder under the die. However, the effect is relatively weak.

The PVU structure gives higher temperature compared to the CVU structure because of the small effect of the heat spreading in the continuous copper layer in the latter.

In the CAR structure, the temperature profile is obtained by adding a constant temperature rise (corresponding to a simple thermal resistance model of the solder layer) to the temperature distribution of the relevant area of copper surface. This is valid because the solder layer is very thin and its thermal conductivity is low, so there is little thermal spreading, and it can be well approximated as a thermal resistance. It is observed that there is a very close match between the temperature profiles of the CAU and the CAR structures confirming this assumption.

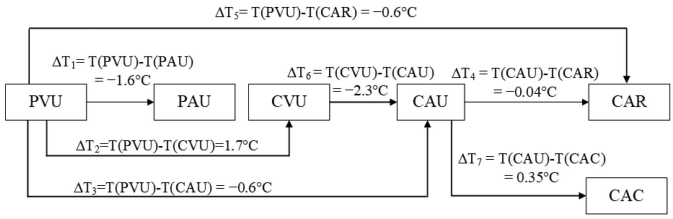

Fig. 11. Temperature differences between different structures at the midpoint of the line AB ($N_m = N_n = 200$ for CAC RNLF).

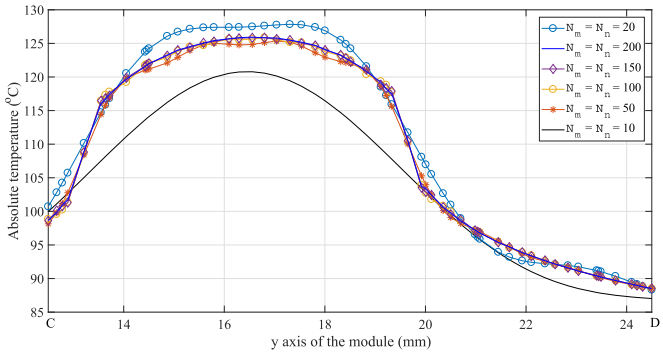

Fig. 12. Temperature profiles along the line CD produced by the RNLF method for a different number of harmonics.

The temperature profile given by the PVU structure matches very closely with those of the CAU structure, the CAR structure, and the CAC structure in the middle region of the die. However, at the both ends of the region of our interest, the CAU and the CAR structures differ from the PVU structure by approximately 4.1°C and the shape of the temperature profile of the PVU structure is different from those of the CAR and the CAU structures.

Fig. 11 illustrates the differences between the temperature profiles of different structures at the midpoint of AB.

2) Convergence: The Fourier series representation of the temperature contains an infinite number of terms. In practice, a truncated form of the Fourier series is used, which raises the issue of convergence. The function of the temperature field meets Dirichlet's condition, so it converges at every point of continuity. Fig. 12 demonstrates the convergence of the temperature profile obtained from the RNLF method (corresponding to CAC structure) along the line CD. It is observed that the temperature profile converges satisfactorily when $N_m = N_n \gtrsim 150$.

C. Design of the Experiment

An experiment is conducted to validate the thermal model using a commercial power module.

1) Mechanical Setup: A liquid cooling bath (not shown in the figure) circulates water through the cooling tubes connected with the heatsink. Fig. 13 shows an arrangement to facilitate the image capturing by an infrared (IR) camera used in the experiment.

The surface of the module is replete with shiny copper traces, semiconductor devices, and wirebonds with the emissivity much lower than 1, which would hinder the IR camera from capturing accurate data. Therefore, black paint is sprayed a number of

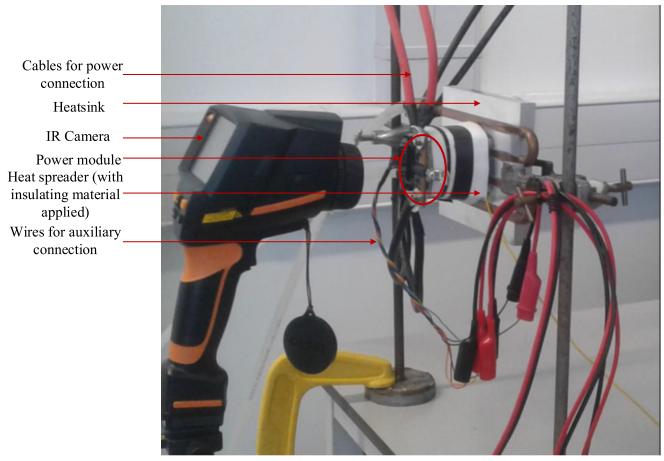

Fig. 13. Experimental setup showing the positioning of the IR camera and the power module.

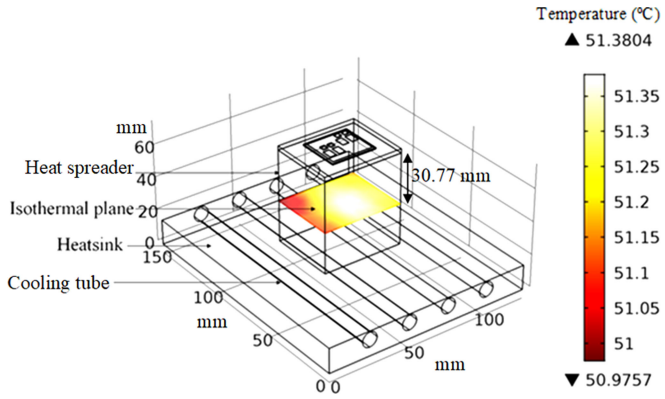

Fig. 14. Model in COMSOL Multiphysics showing the isothermal plane within the heat spreader (note the low temperature difference across the isothermal plane).

times over the top surface of the power module in order to raise the emissivity to close to 1. The value of emissivity setting used in this work is 0.98. A requirement for the experiment is to create an isothermal surface as a boundary condition because the detailed modeling of the liquid-cooled heatsink or the thermal coupling between the power module and the heatsink is not a part of the RNLF method. Therefore, a relatively thick heat spreader made of aluminum alloy is used in the experiment to create this condition by facilitating the heat spreading. The position of the isothermal plane created by the heat spreader is shown in Fig. 14.

A K-type thermocouple is used to measure the temperature of the midpoint of the plane shown in Fig. 14. It gives a reading of 52.6 °C, which is close to the simulation temperature of 51.4 °C. Therefore, in this work, 52.6 °C is considered the temperature of the isothermal plane.

2) Electrical Setup (See Fig. 15): A dc power supply is used as a current source. The MOSFETs are held on continuously using a constant $V_{gs} = 20$ V. The load current is 75 A and is assumed to be shared equally between the parallel-connected MOSFETs. Measuring the V_{ds} of the MOSFETs, it is calculated that $P_{\text{MOSFET 1}} = P_{\text{MOSFET 2}} = 63.75$ W and $P_{\text{MOSFET 3}} = P_{\text{MOSFET 4}} = 76.87$ W.

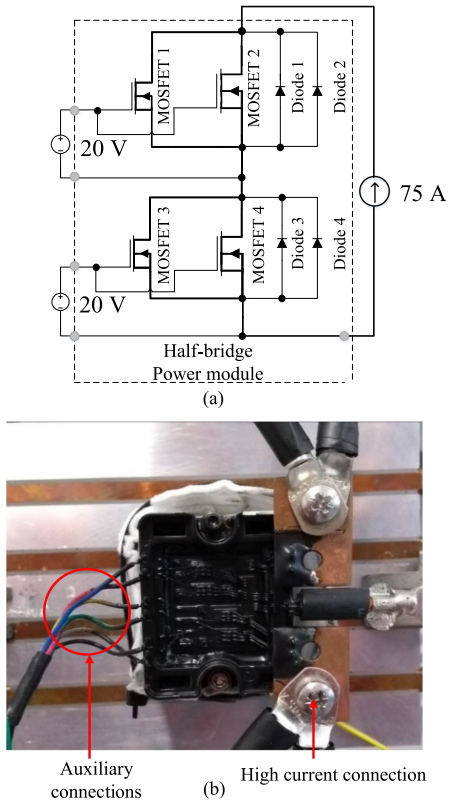

Fig. 15. (a) Schematic diagram of the circuit of the experiment (current path shown in bold). (b) Front view of the module with the Matt black paint applied.

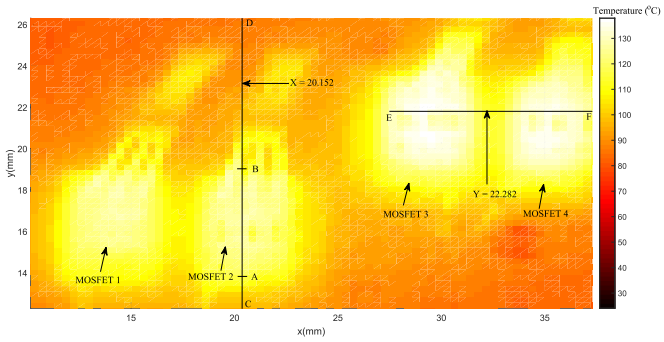

Fig. 16. Thermal image captured by the IR camera showing lines AB, CD, and EF (camera is a Testo-1i with an emissivity setting of 0.98).

D. Comparison Among the Experiment, the RNLF Method, and the COMSOL FEM (PVU) Model

Fig. 16 shows the experimental temperature distribution in the region of interest. Figs. 18 and 19 show the comparisons between the experiment, the RNLF method and the COMSOL FEM (PVU) model along the lines CD and EF. The error between the experiment and the model or simulation at the center of a MOSFET is given by

$$e = \frac{T_{\text{ref}} - T_{\text{test}}}{T_{\text{ref}} - 52.6\,^{\circ}\text{C}} \tag{31}$$

where $T_{\text{ref}} = T_{\text{exp}}$ for the first two error columns and $T_{\text{ref}} = T_{\text{FEM}}$ and $T_{\text{test}} = T_{\text{RNLF}}$ for the last column of Table III.

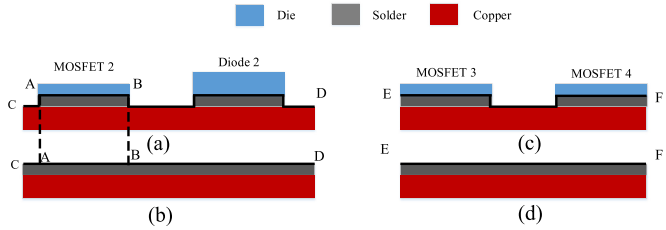

Fig. 17. (a) Side views of the lines AB and CD corresponding to COMSOL FEM (PVU) model. (b) Side views of lines AB and CD corresponding to the RNLF method. (c) Side view of line EF corresponding to the COMSOL FEM (PVU) model. (d) Side view of line EF corresponding to the RNLF method.

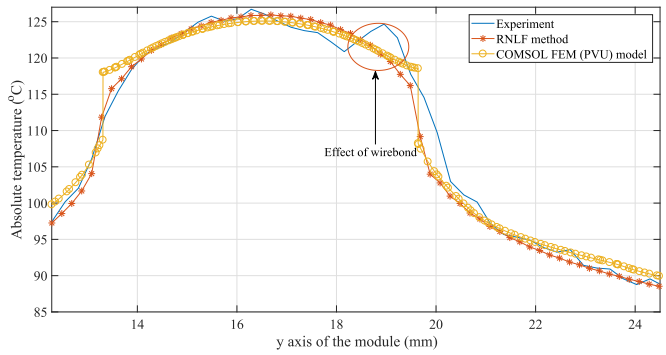

Fig. 18. Comparison among the experiment, the RNLF method, and the COMSOL FEM (PVU) model along line CD ($N_m = N_n = 200$ for RNLF).

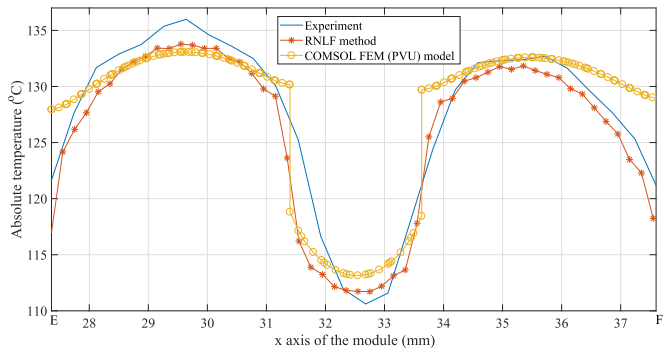

Fig. 19. Comparison among the experiment, the RNLF method, and the COMSOL FEM (PVU) model along line EF ($N_m = N_n = 200$ for RNLF).

In Figs. 18 and 19, the graphs obtained from the RNLF method and COMSOL simulation (PVU) closely match with the corresponding experimental graphs, especially in the middle regions of the MOSFETs. In Fig. 18, a peak is observed at the right edge due to the wirebond.

V. Conclusion

A Fourier-based method for the steady-state thermal modeling of a rectangular N-layer structure is presented. An excellent matching is observed between the surface temperature of a practical power module and that generated by the RNLF method, despite the several simplifications to the structure required to make the RNLF method applicable. This relatively simple method can be used to accurately estimate the maximum junction temperature of semiconductor devices and so may be particularly useful for the fast and robust design and optimiza-

TABLE III
COMPARISON AMONG THE EXPERIMENT, THE COMSOL FEM (PVU) MODEL, AND THE RNLF METHOD

MOSFET No.	Exp. (°C)	FEM (°C)	RNLF (°C)	Error (%) Exp. to FEM	Error (%) Exp. to RNLF	Error (%) FEM to RNLF
2	126.7	125.1	125.9	2.16	1.10	−1.10
3	136.0	133.1	133.8	3.44	2.64	−0.87
4	132.4	132.6	131.8	−0.25	0.75	−1.00

tion of the power module structure and layout. The optimization process is potentially made simpler because the RNLF method is smooth with dimensional changes (unlike other techniques such as the FEM) and is computationally efficient when evaluating only a few point temperatures. This model may also be used to carry out a sensitivity analysis by perturbing the geometrical dimensions and thermal properties of the different layers. This model might further be used to estimate the thickness or thermal conductivity of a particular material (the thermal grease layer for example) given a surface temperature profile found experimentally. Although the focus of this paper has been on power electronic modules, the RNLF method may find other applications in layered structures, assuming that suitable simplifications can be made in these cases.

ACKNOWLEDGMENT

The authors would like to thank S. Bontemps of Microsemi Power Module Products for supplying the sample SiC MOSFET power module and corresponding dimensions and material properties used in this paper.

REFERENCES

[1] F. Masana, "A new approach to the dynamic thermal modelling of semiconductor packages," *Microelectron. Rel.*, vol. 41, no. 6, pp. 901–912, 2001.
[2] F. Masana, "Thermal characterisation of power modules," *Microelectron. Rel.*, vol. 40, no. 1, pp. 155–161, 2000.
[3] S. S. Wen and G.-Q. Lu, "Finite element modeling of heat transfer and thermal stresses for three-dimensional packaging of power electronics modules," in *Proc. 3rd Int. Power Electron. Motion Control Conf.*, 2000, vol. 1, pp. 496–501.
[4] P. L. Evans, A. Castellazzi, and C. M. Johnson, "Automated fast extraction of compact thermal models for power electronic modules," *IEEE Trans. Power Electron.*, vol. 28, no. 10, pp. 4791–4802, Oct. 2013.
[5] A. Raciti and D. Cristaldi, "Thermal modeling of integrated power electronic modules by a lumped-parameter circuit approach," in *Proc. AEIT Annu. Conf.*, Oct. 2013, pp. 1–6.
[6] A. S. Bahman, K. Ma, P. Ghimire, F. Iannuzzo, and F. Blaabjerg, "A 3-D-lumped thermal network model for long-term load profiles analysis in high-power IGBT modules," *IEEE J. Emerg. Sel. Topics Power Electron.*, vol. 4, no. 3, pp. 1050–1063, Sep. 2016.
[7] M. Musallam and C. M. Johnson, "Extraction of efficient thermal models for life limiting interfaces in power modules," in *Proc. 5th Int. Conf. Integr. Power Electron. Syst.*, Mar. 2008, pp. 1–5.
[8] M. J. Whitehead and C. M. Johnson, "Determination of thermal cross-coupling effects in multi-device power electronic modules," in *Proc. 3rd IET Int. Conf. Power Electron., Mach. Drives*, Apr. 2006, pp. 261–265.
[9] A. W. K. L. Balents, R. D. Gold, and W. R. Peterson, "Design considerations for power hybrid circuits," in *Proc. Int. Hybrid Microelectron. Symp.*, Oct. 1969, pp. 323–344.
[10] D. P. Kennedy, "Spreading resistance in cylindrical semiconductor devices," *J. Appl. Phys.*, vol. 31, no. 8, pp. 1490–1497, 1960.
[11] A. G. Kokkas, "Thermal analysis of multiple-layer structures," *IEEE Trans. Electron Devices*, vol. ED-21, no. 11, pp. 674–681, Nov. 1974.
[12] G. N. Ellison, "Maximum thermal spreading resistance for rectangular sources and plates with nonunity aspect ratios," *IEEE Trans. Compon. Packag. Technol.*, vol. 26, no. 2, pp. 439–454, Jun. 2003.
[13] Y. S. Muzychka, J. R. Culham, and M. M. Yovanovich, "Thermal spreading resistance of eccentric heat sources on rectangular flux channels," *ASME. J. Electron. Packag.*, vol. 125, no. 2, pp. 178–185, Jun. 2003.
[14] Y. S. Muzychka, K. R. Bagnall, and E. N. Wang, "Thermal spreading resistance and heat source temperature in compound orthotropic systems with interfacial resistance," *IEEE Trans. Compon., Packag., Manuf. Technol.*, vol. 3, no. 11, pp. 1826–1841, Nov. 2013.
[15] G. N. Ellison, "Thermal analysis of microelectric packages and printed circuit boards using an analytic solution to the heat conduction equation," *Adv. Eng. Softw.*, vol. 22, no. 2, pp. 99–111, 1995. [Online]. Available: http://www.sciencedirect.com/science/article/pii/096599789400032E
[16] A. D. J. Geer and B. Sammakia, "Heat conduction in multilayered rectangular domains," *ASME. J. Electron. Packag.*, vol. 129, no. 4, pp. 440–451, Apr. 2007.
[17] D. Guan, M. Marz, and J. Liang, "Analytical solution of thermal spreading resistance in power electronics," *IEEE Trans. Compon., Packag., Manuf. Technol.*, vol. 2, no. 2, pp. 278–285, Feb. 2012.
[18] I. R. Swan, A. T. Bryant, and P. A. Mawby, "Fast thermal models for power device packaging," in *Proc. IEEE Ind. Appl. Soc. Annu. Meeting*, Oct. 2008, pp. 1–8.
[19] I. Swan, A. Bryant, P. A. Mawby, T. Ueta, T. Nishijima, and K. Hamada, "A fast loss and temperature simulation method for power converters, part II: 3-D thermal model of power module," *IEEE Trans. Power Electron.*, vol. 27, no. 1, pp. 258–268, Jan. 2012.
[20] M. N. Ozisik, *Heat Conduction*, 1st ed. New York, NY, USA: Wiley, 1980.

Khaled Redwan Choudhury received the B.Sc. degree in electrical and electronic Engineering from the Bangladesh University of Engineering and Technology, Dhaka, Bangladesh, in 2011, and the M.Sc. degree in electrical technology for sustainable and renewable energy systems from the University of Nottingham, U.K., in 2012. He is currently working toward the D.Phil. degree with the University of Oxford, U.K.

His research interests include power electronics, control systems, thermal modeling of power electronic systems, and renewable energy.

Daniel J. Rogers (M'09) received the M.Eng. and Ph.D. degrees in electrical and electronic engineering from Imperial College London, U.K., in 2007 and 2011, respectively.

He is currently an Associate Professor with the Department of Engineering Science, University of Oxford, U.K. He conducts research in collaboration with industry and is an investigator on U.K. Engineering and Physical Sciences Research Council research projects in the areas of power electronics, grid-scale energy storage, microgrids, and high-voltage direct-current transmission. His research interests include the use of medium- and large-scale power electronic systems to create flexible electrical networks capable of taking advantage of a diverse range of generation and storage technologies.